Chemical Science

Accepted Manuscript

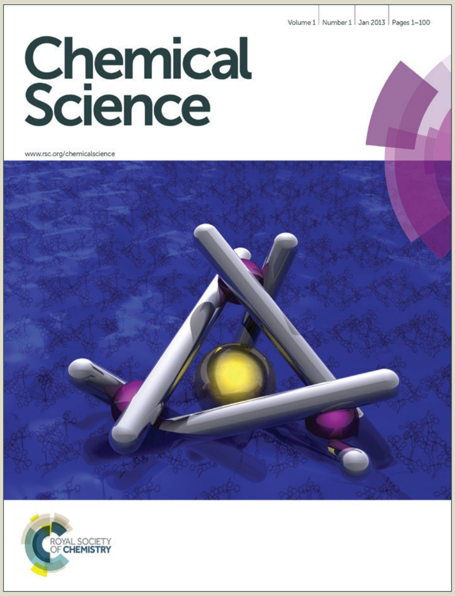

ROYAL SOCIETY OF CHEMISTRY

www.rsc.org/chemicalscience

Mechanistic Insights on the Reductive Dehydroxylation Pathway for the Biosynthesis of Isoprenoids Promoted by the IspH Enzyme

Safwat Abdel-Azeim, Abdesslem Jedidi, Jorg Eppinger, and Luigi Cavallo *

King Abdullah University of Science and Technology, KAUST Catalysis Research Center, Physical Sciences and Engineering Division, Thuwal 23955-6900, Saudi Arabia. Email: luigi.cavallo@kaust.edu.sa

ABSTRACT: Here, we report an integrated quantum mechanics/molecular mechanics (QM/MM) study of the bio-organometallic reaction pathway of the 2H$^+$/2e$^-$ reduction of (*E*)-4-hydroxy-3-methylbut-2-enyl pyrophosphate (HMBPP) into the so called universal terpenoids precursors isopentenyl pyrophosphate (IPP) and dimethylallyl pyrophosphate (DMAPP), promoted by the IspH enzyme. Our results support the viability of the bio-organometallic pathway from rotation of the OH group of HMBPP away from the [Fe$_4$S$_4$] cluster at the core of the catalytic site, to be engaged in a H-bond with Glu126. This rotation is synchronous with π-coordination of the C2=C3 double bond of HMBPP to the apical Fe atom of the [Fe$_4$S$_4$] cluster. Dehydroxylation of HMBPP is triggered by a proton transfer from Glu126 to the OH group of HMBPP. The reaction pathway is completed by competitive proton transfer from the terminal phosphate group to the C2 or C4 atom of HMBPP.

Introduction.

Malaria and tuberculosis are plagues threatening the health of millions of humans every year.[1, 2] This has spurred intense research programs targeting the development of drugs against these diseases. One of the most promising strategies is focused on blocking the biosynthesis of isoprenoids in the pathogen bacteria. This strategy is possible because there are two main pathways for the biosynthesis of isoprenoids. The first is the non-mevalonate pathway, known as the methylerythritol phosphate (MEP) pathway, the second is the mevalonate (MVA) pathway.[3] The MEP pathway is operative in the overwhelming majority of eubacteria, including key pathogens, while the MVA pathway is operative in archaebacteria, most eukaryotes and fungi. Thus, blocking the MEP pathway would allow inhibiting isoprenoids biosynthesis in the pathogens bacteria without affecting their biosynthesis in humans.

In this scenario, the greatest attention has been focused on two enzymes at the end of the sequential cascade of the MEP pathway, namely the IspG and IspH enzymes. Both enzymes use a [Fe$_4$S$_4$] iron-sulfur cluster as a cofactor. The IspH enzyme, focus of this work, is functional to the 2H$^+$/2e$^-$ reduction of (*E*)-4-hydroxy-3-methylbut-2-enyl pyrophosphate (HMBPP) into the so called universal terpenoids precursors isopentenyl pyrophosphate (IPP) and dimethylallyl pyrophosphate (DMAPP), see Scheme 1.

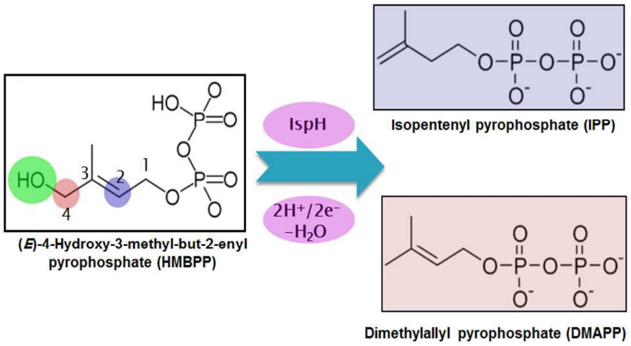

Scheme 1: Conversion of HMBPP into IPP and DMAPP by IspH.

The structure of IspH consists of three domains with similar folding and an overall clover-like shape. The [Fe$_4$S$_4$] cofactor is located inside the central cavity of the enzyme (see Figure 1). Each domain comprises four strands (β1-β4) arranged in a central parallel β sheet surrounded by α-helices α1-α3. The cluster is coordinated by the highly conserved cysteines 12, 96 and 197, whose presence is fundamental to preserve enzymatic functionality, as evidenced by mutagenesis experiments.[4] The crystallographic structure of IspH complexed with HMBPP reveals a hairpin conformation of the ligand, with the hydroxyl group bounded to the apical iron atom Fe1 of the [Fe$_4$S$_4$]$^{+2}$ cluster (for atom numbering see Figure 2).[5]

As regards the sequence of elementary steps composing the reaction pathway for HMBPP reduction by the IspH enzyme, a number of studies have converged on two distinct mechanisms. The so called Birch-like reduction pathway, and the bio-organometallic pathway, see Scheme 2. In the Birch-like reduction pathway, one electron is transferred from the iron-sulfur cluster to HMBPP, which prompts the rupture of the C-O bond. This converts the C-skeleton of HMBPP into an allyl radical intermediate, which is coordinated to the [Fe$_4$S$_4$] cluster. A second electron transfer, coupled with protonation at different carbons of the allyl moiety (C2 or C4 of HMBPP), gives IPP and DMAPP, respectively, see scheme 2A.[6-9]

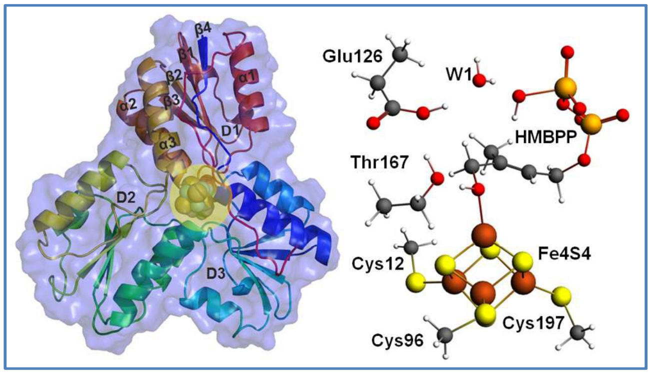

Figure 1: IspH secondary structure, with a sphere representation of the iron-sulfur cluster and of the HMBPP substrate (highlighted in yellow circle). Stick and ball view of the iron-sulfur cluster, coordinated cysteinates, HMBPP, Thr167, Glu126 and bridged water molecule.

The most likely bio-organometallic pathway starts with dissociation and rotation of the OH group of HMBPP away from the apical Fe1 atom, to be engaged in a H-bond with the universally conserved Glu126. Synchronous to this rotation, there is a small slippage of the C2=C3 double bond of HMBPP to π-coordinate to the Fe1 atom, see Scheme 2B. This structural rearrangement triggers dehydroxylation of HMBPP, assisted by a proton transfer from Glu126, and conversion of the C-skeleton of HMBPP into an allyl moiety π-coordinated to the Fe1 atom. Then, a second electron transfer associated with protonation of the allyl intermediate to form IPP and DMAPP completes the reaction pathway. [10, 11,12]

According to the bio-organometallic pathway, rotation of the 4-OH group to engage in a H-bond with Glu126 and π-coordination of the C2=C3 bond to the $[Fe_4S_4]$ cluster is fundamental. [5] Support to this proposal is from mutagenesis experiments, which demonstrated that replacing Glu126 by a glutamine reduces enzymatic activity to a negligible 0.3%.[11, 13] Incidentally, this also suggested that besides maintaining the hydrogen bond network around the catalytic site, Glu126 also plays an important catalytic role.

In addition to the aforementioned evidences, electron paramagnetic resonance spectroscopy and crystallographic studies identified paramagnetic reaction intermediates using Glu126Ala and Glu126Gln mutants. These mutants present the OH group of HMBPP rotated away from the Fe1 atom of the $[Fe_4S_4]$ cluster, and a weak π-complex between the Fe1 atom and the C2=C3 double bond of HMBPP, intermediate II in Scheme 2B. Further, similar studies on the wild-type IspH allowed characterizing intermediate IV of Scheme 2B. Finally, free radical formation was not detected during the reaction steps, which was taken as an evidence against the occurrence of the Birch reduction mechanism. [14]

Despite the available data converge in favor of the bio-organometallic mechanism, a clear understanding of the elementary steps characterizing this mechanism are still missing. To shed light on these points, which would further support the viability of bio-organometallic mechanism, we performed N-layered integrated molecular orbital and molecular mechanics (ONIOM) calculations.[15-17]

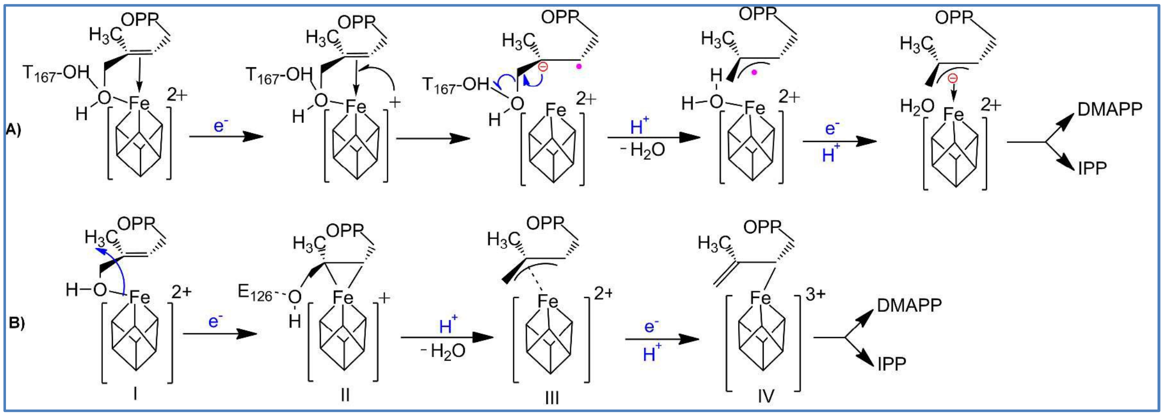

Scheme 2: Reaction pathways and intermediates proposed to be involved in the IspH catalysis. A is Birch-like mechanism, B is the most accepted bio-organometallic mechanism

This approach has already proved reliable for the characterization of the electronic properties of large biological systems.[18-21] The modeling of metallo-enzymes containing magnetic molecules like the iron-sulfur cluster of IspH presents a further challenge due to the presence of the antiferromagnetic coupling between the iron atoms. This kind of coupling can be well described using the broken symmetry (BS) approach developed by Noodleman,[22, 23] and we have adopted it here. Indeed, the BS approach has been successfully used to study the electronic properties of iron-sulfur clusters.[24-29] Finally, to investigate the convergence of the calculations with respect to the size of the quantum mechanics model used to simulate the active site, we performed DFT+U calculations on an extended model up to 456 atoms.

Results and Discussion.

Optimized structure of the HMBPP-coordinated complex.

In the crystallographic structure the Fe-S distances vary significantly, with the apical Fe1 atom showing the longest Fe–S bond lengths, with an average Fe1–S distance of 2.38 Å, whereas the Fe2 atom displays significantly shorter Fe–S bond lengths, with an average Fe2-S distance of 2.20 Å, consistent with a ferric character of the Fe2 atom. The Fe3–S and Fe4–S bond lengths assume intermediate values, with a mean Fe–S distance of 2.28 ±0.04 Å, suggesting mixed valence for these atoms. An extensive list of experimental distances compared with the analogous distances in the ONIOM optimized (B3LYP/TZVP:Amber) structures using model M1 of the HBBPP-coordinated IspH in the oxidized $[Fe_4S_4]^{2+}$ state in different BS states are reported in Table S1.

Analysis of structures optimized using different spin couplings between the Fe centers indicates that, on the average, the DFT Fe–S distances are elongated compared to the corresponding distance in the crystallographic structure, with the exception of the Fe1-S distance, which is instead reproduced accurately. The general trend we observed is that longer Fe-S bond lengths were obtained for Fe1 and Fe4, with an average value of 2.38 Å, compared to Fe2 and Fe3, with an average value of 2.33 Å. Nevertheless, as indicated by Blachly et al.,[30] the main conclusion is that the DFT optimized structures are unable to reproduce the asymmetry observed experimentally, with all the Fe–S distances in the restricted 2.33-2.38 Å range. As final remark, we notice that the optimized Fe-S_{Cys} bonds are in general better agreement with the X-ray values, compared to the Fe-S-Fe bonds, which is not surprising considering that the Fe-S-Fe bonds have to mediate spin coupling between the Fe centers.

Moving to the Fe-Fe bond distances, all of them are elongated in comparison to the experimental distances. Nevertheless, considering these are distances between atoms not directly bonded, the agreement of the optimized structure with the X-ray structure is satisfactory. Indeed, focusing on the most stable BS state, the largest deviation between the DFT and the crystallographic distances amounts to 0.20 Å only for the Fe2-Fe3 distance, which is reasonably small and definitely much smaller than the deviation reported for the Fe-Fe distance in similar systems.[31, 32]

To check further for the impact of the computational protocol on the optimized geometries, test calculations were performed by adopting the ONIOM-EE scheme in the geometry optimization. The minimal deviation between the ONIOM-ME and ONIOM-EE geometries, with the Fe-S and Fe-Fe distances differing by less than 0.02 and 0.05 Å, see Table S3, clearly indicates that the protocol for the electrostatic coupling between the QM and MM parts has minimal impact on the optimized structures.

The overall good agreement of the ONIOM-ME optimized structure of model M1 with the crystallographic structure, and the stability of the optimized structure relative to the electrostatic coupling between the QM and MM parts suggests that geometries optimized at the ONIOM-ME level using model M1 can offer valuable structural information on species for which an experimental structure is not available, including those involved in reactivity. However, for better energetics we performed single point ONIOM-EE energy calculations on the ONION-ME optimized geometries.

Geometry optimizations of model M1 were also performed in the reduced spin state $[Fe_4S_4]^+$ with different spin couplings, see the SI for details. Focusing on the most stable BS state, see Table S3, we observed further elongation of the Fe-S bond lengths with respect to the same structure optimized in the oxidized $[Fe_4S_4]^{2+}$ state, with an average Fe-S value of 2.36 Å against 2.35 Å of the oxidized state, which is at the end a minimal change considering the addition of one electron into the model. NPA analysis indicates that the added electron is essentially located on the $[Fe_4S_4]$ cluster (see SI).

HMBPP dehydroxylation.

In the crystallographic structure of the IspH/HMBPP complex, the 4-OH group of the substrate is coordinated to the apical Fe1 atom. The first step proposed along the bio-organometallic mechanism consists in a conformational rearrangement of the substrate that, through rotation around the C3-C4 bond, replaces the Fe1-OH interaction by π-coordination of the C2=C3 double bond. Support to this scenario was provided recently by HYSCORE experiments resulting in a very weak ^{17}O hyperfine coupling constant of 1 MHz. This indicated a weak to non-existing Fe-4OH interaction, since Fe-O bonding in other Fe-S clusters containing enzymes usually exhibits ^{17}O hyperfine coupling constants in the 8-15 MHz range.[14]

To shed light on the feasibility of this rearrangement of the substrate, we performed ONIOM calculations using the most stable BS state of model M1. A reduced $[Fe_4S_4]^+$ state of the cluster was considered, since this is the experimentally supported active species.[14] Initially, we considered Glu126 to be deprotonated. Relaxed scan of the Fe1-O distance was carried out to simulate rotation of 4-OH group away from the apical Fe1 atom and promote coordination of the C2=C3 double bond, see Figure S3. The structure highest in energy along the scan was used to locate the transition state for this rearrangement of the substrate, **TS1**, and its first order saddle point character at the ONIOM-ME level was verified through frequency calculations. According to these calculations, the 4-OH group undergoes this rotation with a barrier of 9.7 kcal/mol, a result basically confirmed by the single point ONIOM-EE calculations, which result in a barrier of 13.0 kcal/mol. Relaxation of transition state **TS1** on the product side leads to the expected η^2-complex **I1**, only 0.7 kcal/mol below **TS1** at the ONIOM-ME level, while at the ONIOM-EE level **I1** is predicted to be 4.7 kcal/mol above **TS1**. The structure of intermediate **I1** shows the C2=C3 bond well-coordinated to the apical Fe1 atom, with the Fe1-C2 and Fe1-C3 distances around 2.27 Å, while the 4-OH group is 3.58 Å away from the Fe1 atom see Figure 2.

In short, these calculations converge in suggesting that rotation of the 4-OH group is facile, with a barrier around 10-15 kcal/mol, and that the product of this rotation, the η^2-complex **I1**, is clearly less stable than the starting 4-OH coordinated complex. At the same time, they highlight that the absolute numbers have to be taken *cum grano salis*, since the ONIOM-EE method predicts the ONIOM-ME geometry of intermediate **I1** to be less stable than that of the preceeding transition state **TS1**. The impact of the chosen computational approach on the energetics of the reaction is discussed in a dedicated section, see below. Next we modeled dehydroxylation of HMBPP by elongating the C4-O4 bond, still in presence of the unprotonated Glu126. The located transition state **TS2** and the following intermediate **I2** are about 75 and 50 kcal/mol above the initial reactant **R** with both the ONIOM-ME and ONIOM-EE methods, see Figure 2, which rules out this pathway.

Considering the experimentally proved crucial role of Glu126 in promoting catalysis,[11, 13] we modeled the same steps in presence of a protonated Glu126, see Figure 2 and S4. First, we modified the hydrogen bond network around Glu126 to accommodate the added proton. Several geometry optimizations were performed to search the most stable and appropriate orientation enabling the reaction to occur. In the most stable conformation the proton of Glu126 is oriented towards water WT1, while one of the protons of water WT1 is oriented towards the phosphate group. Incidentally, this network of hydrogen bonds also results in a suitable orientation for a H-transfer from the phosphate to the substrate.

As first step we recalculated the energy required for rearranging the substrate from the 4-OH coordinated species **R**, to the C2=C3 coordinated intermediate **I1**, through transition state **TS1**. Also in presence of a protonated Glu126, rotation of the 4-OH group is an easy process, with a barrier around 10 kcal/mol at both the ONIOM-ME and ONIOM-EE level. This is reasonable, as this process does not perturb the hydrogen bond network of the active site considerably. Next, we located transition state **TS2**, corresponding to cleavage of the C4-OH bond, and we found a much lower barrier, 7.7 and 28.7 kcal/mol at the ONIOM-ME and ONIOM-EE levels, relative to the barrier of about 75 kcal/mol in presence of a deprotonated Glu126. Further, the protonation of Glu126 also results in a much more stable intermediate **I2**, see Figure 2. In this case, the ONIOM-ME and ONIOM-EE result in a clear discrepancy, which again indicates that energies have to be taken with caution.

The much better energetics for the C4-OH cleavage in presence of a protonated Glu126 is due to a concerted transfer of the acidic proton of Glu126 to water WT1, while one of the protons of water WT1 is transferred to the leaving 4-OH group, (see Figure S2) which is then leaving the substrate as a water molecule rather than a hydroxyl, as in presence of a deprotonated Glu126. In other words, it is the acidity of Glu126 that triggers the C4-O bond cleavage through the mediating role of the WT1 water molecule. In line with this scenario, this bridged water molecule is well conserved in the available crystallographic structures of IspH (PDB codes: 3KE8, 3KE9, 3KEL[33], 3F7T,[4] 3SZO, 3SZL[5], 3URK, 3UTC, 3UV3, 3UWM, 3MUX, 3UV6 3UV7[34], and 4H4D[35]).

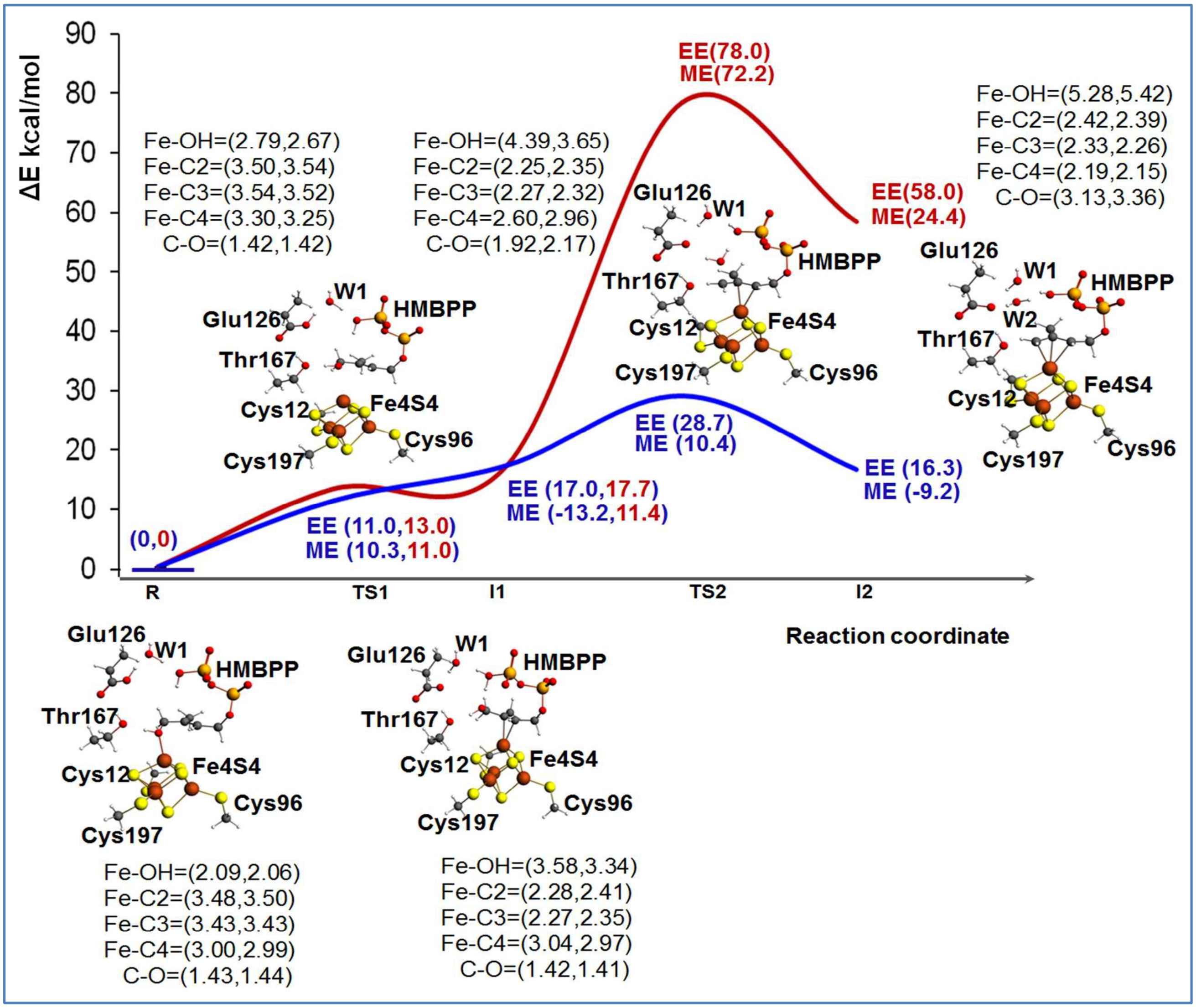

Figure 2: ONIOM (B3LYP/TZVP:Amber) reaction profile of the first step of the IspH promoted reactivity, corresponding to rotation and dehydroxylation. The red line corresponds to the case of deprotonated Glu126, while the blue line corresponds to the case of the protonated Glu126. ME energies correspond to mechanical embedding with model M1, which is the mode used in the geometry optimization. EE energies correspond to electrostatic embedding evaluated through single point energy calculations with model M2 using

geometries from model M1. Stationary points are represented in balls and sticks. Key bond distances are reported in parenthesis, the first value is for the profile of deprotonated Glu126 and the second value is for the profile of the protonated Glu126.

In addition, we also checked if the proton transfer assisting the C4-OH cleavage could occur from the properly oriented OH group of the phosphate, rather than from Glu126. To this end, we first transferred the proton from the phosphate to the 4-OH group and relaxed the (Glu126 protonated) structure while constraining the distance between the 4-O atom and the transferred proton to 0.98 Å, to induce formation of intermediate **I2**. In the constrained optimized structure we observed an elongation of the C4-O bond, 1.46 Å, still the bond is not broken. Relaxing the structure with the constraint removed resulted in the proton being transferred back to the phosphate group and the C4-O bond reformed again. This suggests that the phosphate cannot act as the promoter of the C4-O bond cleavage. As another possibility, we also checked if the terminal phosphate group could have two O atoms protonated (in this case Glu126 is deprotonated), see Figure S10. Starting from this di-protonated phosphate we located again **TS2**, corresponding to the dehydroxylation step. The calculated reaction barrier from the starting complex **R** is still high, around 70 kcal/mol, and intermediate **I2** of high energy, around 39.0 kcal/mol above **R**, see Figure S9, ruling out also this possibility.

Finally, despite the experimental evidences that the active spin state is the reduced $[Fe_4S_4]^+$ state, we also investigated the reaction profile using the oxidized state $[Fe_4S_4]^{2+}$. However, calculations indicate that intermediates **I1** and **I2** are high in energy, 27.4 and 34.5 kcal/mol above **R** at the ONIOM-EE level, makes this possibility less likely to happens. These results suggest that rotation and the dehydroxylation of the 4-OH group are much easier in the reduced state than the oxidized one. This suggests that the electron transfer (ET) to the cluster, reducing the $[Fe_4S_4]^{2+}$ state to the $[Fe_4S_4]^+$ state should occur before rotation of the 4-OH group.

In conclusion our analysis indicates that dehydroxylation can occur only on the reduced $[Fe_4S_4]^+$ state in presence of a protonated Glu126. For this reason, in the following we focus on a more detailed analysis of the **I1** and **I2** intermediates along this reaction pathway.

To have a better understanding of the energy difference between 4-OH coordination and C2=C3 coordination, we also investigated the simple model shown in Figure S1. This model allows focusing on the core interaction between the cluster and the substrate, without the complication of the surrounding groups. Calculations were performed in the gas-phase, and both for the $[Fe_4S_4]^{2+}$ and $[Fe_4S_4]^+$ states (see details reported in SI). The optimized geometries are reported in Table S14. According to calculations, the C2=C3 coordinated geometry is favored by -0.1 and -10.7 kcal/mol in the $[Fe_4S_4]^{2+}$ and $[Fe_4S_4]^+$ states, respectively. This is in line with calculations on the M2 model discussed previously, where we found that intermediate **I1** is more competitive with 4-OH coordination in the reduced state, rather than in the oxidized state.

Analysis of the NPA charges and spin densities of the QM region along the reaction pathway in the case of the catalytically active species corresponding to the protonated Glu126 and reduced $[Fe_4S_4]^+$ state indicates that there is significant change in the cluster total charge and spin density between the 4-OH or C2=C3 coordinated species **R** and **I1**, rather than from **I1** to **I2**, as indicated by NPA charges of -2.03e, -1.54e and -1.24e in **R**, **I1** and **I2**, and spin densities of 0.95, 1.24e and 1.39e. Indeed, these results indicate that most of the changes in the electronic structure of the cluster are due to the rotation of the 4-OH group, which act as a donor to increase electron density on the cluster, while the C=C double bond in **I1** and the allyl moiety in **I2** have π* orbitals available to accept back-donation from the cluster. Consequently, the 4-OH rotation step results in a clear transfer of about 0.5e the cluster from the substrate in **I1**, and an additional transfer of about 0.3e in the dehydroxylation step **I1** to **I2**, consistently with formation of a more acidic π* orbital in the allyl moiety of **I2**. Finally, the overall NPA charge of the allyl group in **I2** amounts to 0.43e, which indicates that the allyl group has a substantial neutral character.

Analysis of the molecular orbitals of **I2**, in the enzymatically active reduced state with a protonated Glu126, shows more communication between the substrate and the cluster. For instance, the SOMO is concentrated on the iron cluster while the LUMO is localized on the allyl moiety, which can act as an electron acceptor in the following electron transfer and protonation steps, see Figure 3. A complete list of the frontier orbitals of **I2** in the protonated, deprotonated Glu126, reduced and the oxidized cluster are reported in SI.

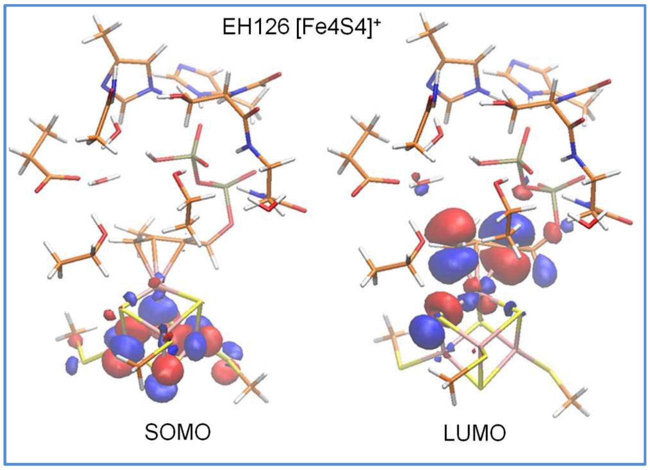

Figure 3. Frontier molecular orbitals of intermediate **I2** of the reduced $[Fe_4S_4]^+$ state in presence of a protonated Glu126. The molecular orbital isosurfaces are plotted at 0.03 a.u.

Further analysis of the NPA charges and of the absolute spin density does not show remarkable difference between the four Fe atoms, with one of them having a clearly different oxidation state, see Figure 6 and Tables S6. In fact, the NPA charges on the Fe atoms in **R**, **I1** and **I2**, range between 1.02 and 1.23e, while the absolute spin density, ranges between 3.35 and 3.68e. This prevents assigning a formal oxidation state (III) to one of the Fe atoms in the 3Fe(II)/1Fe(III) $[Fe_4S_4]^+$ in the cluster reduced state. Finally, we found a remarkable amount of excess α spin density, on the average 0.23e per S atom, also on the bridged sulfide anions. Consistently with similar conclusions reported for [FeFe]-hydrogenases[36, 37] and for model complexes,[38-40] this shows the important role of the sulfur ligands for tuning the redox properties of the iron-sulfur cluster, with the sulfur atom acting like reservoirs of electron density to compensate changes in the electronic state of the cluster.

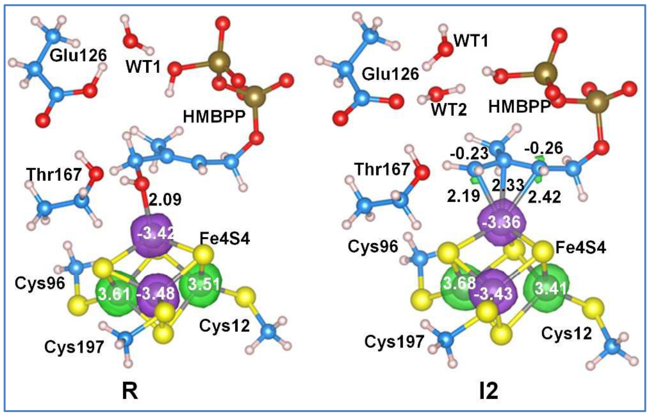

Figure 4: Spin density on the Fe atoms of structures **R** and **I2** along the reaction pathway with $[Fe_4S_4]^+$ cluster in the reduced state. Spin densities are represented by transparent spheres (α: green and β: purple) and are represented at 0.03 u.a. Key bond distances are reported in Å.

NBO analysis does not show any orbital overlap between the apical iron atom and the coordinated carbon moieties in **I1** and **I2**, despite of the short Fe-C distances. We thus extended the analysis on the nature of the Fe-C interaction by calculating the Natural Bond Critical Points (NBCPs).[41] Based on the atom in molecules (AIM) concept, the presence of a CP on the line joining two atoms indicates a chemical bond, while the electron density at the CP measures the strength of the bond. Finally, the sign of the laplacian of the electron density, $\nabla^2\rho(r)$, is a sign of concentration or depletion of electron density, with $\nabla^2\rho(r) < 0$ and > 0 indicating a covalent or ionic character in the bond. [42-44] According to this analysis, the Fe-O and Fe-C interaction in **R**, **I1** and **I2** has a dominant ionic character, since the density at the CP along these bonds is never greater than 0.07 a.u., and the $\nabla^2\rho(r)$ is constantly positive. For comparison, for a strongly covalent bond, as the C4-O bond, the electron density at the CP is 0.2442 a.u, and the $\nabla^2\rho(r)$ is negative (see Table S12). Interestingly, the same analysis performed on the Fe1-S bonds indicates that these bonds also have an ionic character, as suggested by the very low electronic density and positive laplacian at the CP located along these bonds.[45] This is consistent with similar analysis on methane monooxygenases,[46] and with the dominant ionic interaction reported for several transition metals complexes. [45, 47-49]

QM/MM convergence and DFT+U calculations

To test the convergence of our results with respect to the size of the QM part in the ONIOM calculations, we compared the energies discussed so far, achieved with model M1, 92 atoms in the QM part, with the ONIOM-ME energies achieved using model M2, 160 atoms in the QM part. These tests indicate that the overall scenario provided by models M1 and M2 is very similar, and using the larger model M2 has no impact on the overall conclusions discussed above, although it is clear that the specific energy values are somewhat dependent on the specific model used. In fact, both models predict a rather small barrier for rotation of the 4-OH group, that dissociation of the C4-OH bond is rate determining, and that the resulting allyl coordinated intermediate **I2** is higher in energy than the starting 4-OH coordinated species **R**, see Figure S7. This is consistent with results of Iwasaki et al. that indicated that the hydrogen bonds established by the backbone peptide tune the electronic structure and the geometry of the Fe_2S_2 cluster in Rieske type proteins,[50] and of model iron-sulfur complexes.[51] Despite this positive test, we wondered if the extension of the hydrogen bond pattern and of the resulting interactions around the iron cluster could affect our conclusions, since in the ONIOM-based calculations we considered only the first protein/water shell around the substrate, and we cut the cluster-bonded cysteines at the Cα-Cβ bond. To shed light on this issue we investigated the larger model M3, 456 atoms, using DFT+U and plane wave calculations, as implemented in VASP, which performs quite well for magnetic molecules.[52] Indeed, earlier studies showed that VASP calculations reproduced G09 results within 0.5 kcal/mol limit of accuracy.[53] Using model M3 we re-optimized the structures along the favored reaction pathway corresponding to the reduced $[Fe_4S_4]^+$ state in presence of a protonated Glu126. To mimic the overall protein structure, geometry optimization of the intermediates was performed by constraining the position of the Cα atoms at the boundaries of the cluster. For the transition states **TS1** and **TS2** we further constrained the breaking Fe-O and C-O distances at the value resulting from the ONIOM G09 calculations discussed above. Comparison between the ONIOM M1 and the DFT+U M3 structures results in RMSD between the heavy atoms smaller than 0.04 Å, see Table S13 for the optimized parameters, which validates all the structural considerations based on the M1 geometries. Further, comparison of the M3 and M2 energy profiles, see Figure S13, shows a very good agreement between the two methods, since the largest deviations are small differences between the relative stability of **TS1** and **I1**, which are predicted to be slightly more stable in DFT+U profile. In short, these tests confirm that our results can be considered converged both in terms of geometries and energies.

Allyl protonation

The last step of the IspH mechanism is the protonation at two different carbon atoms of HMBPP skeleton of intermediate **I2**, namely C2 to produce IPP and C4 to produce DAMPP. To investigate this step we performed two different relaxed scans to simulate the proton transfer from the phosphate group of HMBPP to C2 and C4 (see figure S14). Focusing on the potential energy surface calculated at ONIOM-EE and model M2, protonation at C2 (blue and green) is easier than protonation at C4 (red) (see Figure 5). The reaction barrier for the proton transfer from the phosphate group to C2 is clearly lower (8.3 kcal/mol) than the barrier to protonate C4 (12.1 kcal/mol). This is in good qualitative agreement with the experimental evidence that IspH produces IPP and DAMPP in a 5:1 ratio.[6, 12]

Collapsing the two transition states into the products side, with the substrate still coordinated to the apical Fe1 atom, resulted in kinetic products of limited stability. A much more stable structure, **I5**, was achieved by coordination of the formed water molecule to the apical Fe1 atom. This concerted rearrangement of the products, with a relatively large dislocation of several molecules, is practically impossible to model with static methods, so we did not performed attempts in this direction.

Nevertheless, we remark that protonation at either C2 or C4 from the phosphate tail of the substrate locates an additional formal negative charge on the phosphate. Considering that the phosphate group is located near the protein surface, it is tempting to suggest that solvation could drive the final product outside the HMBPP binding site.

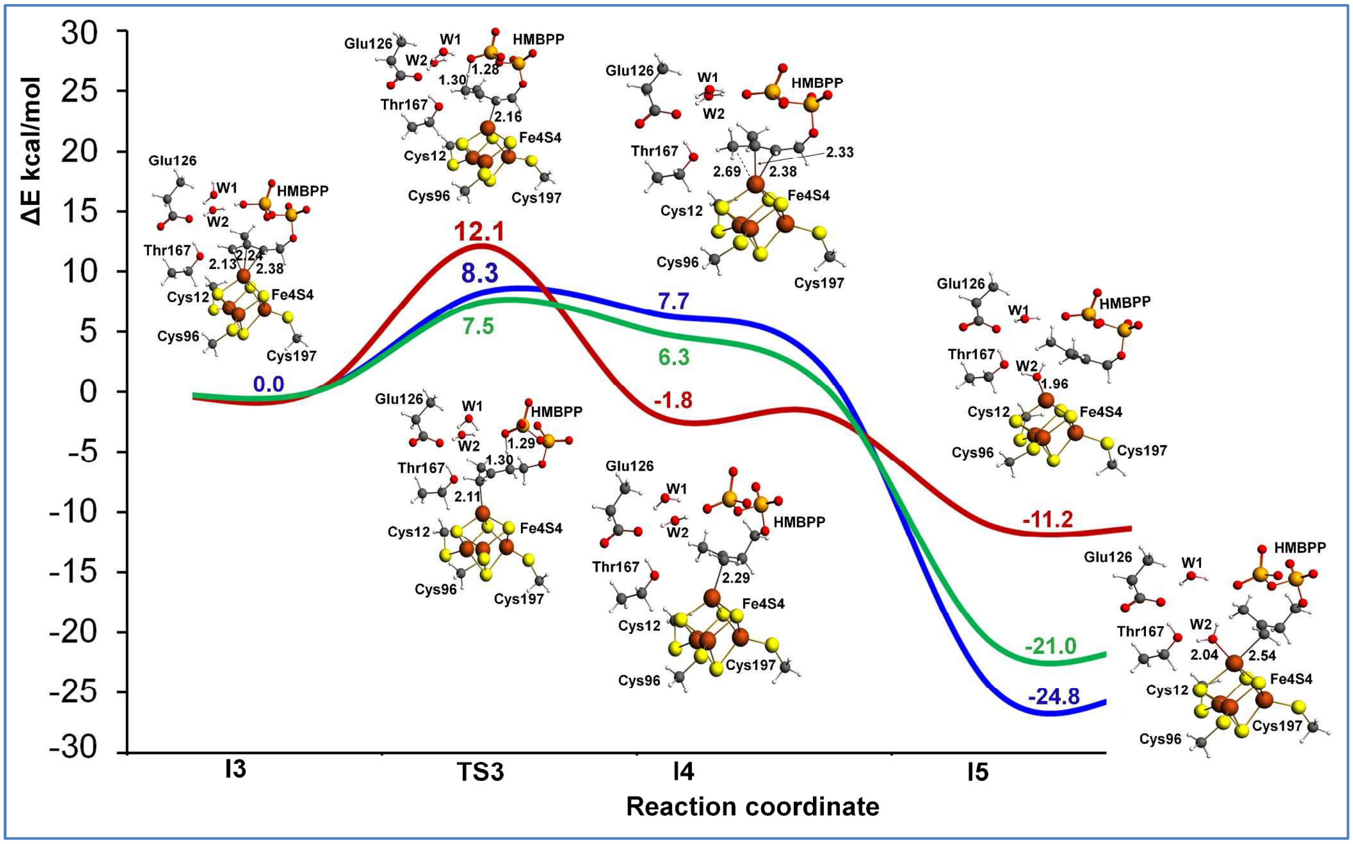

Figure 5: ONIOM (B3LYP/TZVP:Amber)-EE reaction profile of the allyl protonation step. Key bond distances are reported in Å. The red line corresponds to protonation at C4, the blue line to protonation at C2, and the green line to protonation at C2 using the DFT+U approach and M3 model.

Also in this case we recalculated the reaction profile using the larger model M3 and the DFT+U approach to ensure the convergence of the ONIOM results. As in the case of the initial part of the reaction profile, Figure S13, the DFT+U calculations reproduce with high accuracy the ONIOM-EE numbers also for the proton transfer from the phosphate to the allyl moiety of the substrate, which again confirms the convergence of the results with respect to the model size (see figure 5).

A paramagnetic complex is formed upon formal e^-/H^+ transfer in which the iron-sulfur cluster has an oxidation state of $[Fe_4S_4]^{+3}$ which is similar to that involved in the catalysis of the high-potential iron–sulfur protein (HiPIP) family. The LUMOs (LUMO-LUMO+5) of the final products are located on the cluster which are supposed to be populated under further reduction process to activate the cluster (see able S10).

Conclusion

We reported the first computational investigation of the elementary steps of the IspH catalysis using state-of-the-art ONIOM technique coupled with the broken symmetry DFT approach. Further, we have adopted plane wave DFT+U calculations for rescoring some key stationary points already optimized within the ONIOM approach. The main result is that our calculations fully support the bio-organometallic mechanism, while ruling out the Birch-like mechanism, with formation of radical species during the dehydroxylation step.

Focusing on the favored bio-organometallic mechanism, our calculations indicate that the active species involved in the IspH catalysis is the reduced cluster $[Fe_4S_4]^+$. The reduction of the iron-sulfur cluster helps rotation of the 4-OH group of the substrate away from the iron cluster, with π-coordination of the C2=C3 double bond. The rotated OH group is engaged in a H-bond interaction with Glu126. Proton transfer from Glu126, mediated by a conserved water molecule, trigger dehydroxylation of HMBPP with its conversion into a -coordinated allyl moiety involving the C2-C4 atoms of HMBPP. Calculations suggest that these steps can only occur with the iron cluster in a reduced state, due to the high energy of the same intermediates in presence of an iron cluster in the oxidized state. The key role of Glu126 is further demonstrated by the high energy of the dehydroxylation step in case of a deprotonated Glu126. As for protonation of the formed allyl intermediate, our calculations suggest a crucial rearrangement of the active site in order to release the final product. Consistently with experiments, protonation to the C2 and C4 atoms of HMBPP is competitive. Finally, we validated the ONIOM calculations by evaluating the relative energy of the key intermediates along the favored pathway using DFT+U plane wave calculations on a large quantum mechanics model including up to 456 atoms.

As concluding remark, we note that the reaction profile calculated by the ONIOM and DFT+U approaches predicts that dehydroxylation of HMBPP is the rate determining step, in agreement with recent inhibition studies evidencing that (E)-4-mercapto-3-methylbut-2-en-1-yl diphosphate and (E)-4-amino-3-methylbut-2-enyl 1-diphosphate are potent inhibitors of IspH in the nano-molar range. [54, 55] Both molecules are HMBPP analogues, where the 4-OH group is replaced by thiol and amino groups respectively.

Acknowledgments.

This research used the resources of the Supercomputing Laboratory under the project k224 at King Abdullah University of Science & Technology (KAUST) in Thuwal, Saudi Arabia.

Supporting Information Available

Computational methods, further analysis, and Cartesian coordinates of all the species discussed.

Notes and References.

1. World Health Organization. World Malaria Report 2013, WHO Press: Geneva, S., 2013.
2. World Health Organization. World Tuberculosis Report 2013, WHO Press: Geneva, S., 2013.
3. M. Rohmer, Nat. Prod. Rep., 1999, **16**, 565-574.
4. T. Grawert, F. Rohdich, I. Span, A. Bacher, W. Eisenreich, J. Eppinger and M. Groll, *Angew. Chem. Int. Edit.*, 2009, **48**, 5756-5759.
5. I. Span, T. Grawert, A. Bacher, W. Eisenreich and M. Groll, *J. Mol. Biol.*, 2012, **416**, 1-9.
6. F. Rohdich, F. Zepeck, P. Adam, S. Hecht, J. Kaiser, R. Laupitz, T. Grawert, S. Amslinger, W. Eisenreich, A. Bacher and D. Arigoni, *P. Natl. Acad. Sci. U.S.A.*, 2003, **100**, 1586-1591.
7. Y. L. Xiao, Z. K. Zhao and P. H. Liu, *J. Am. Chem. Soc.*, 2008, **130**, 2164-2165.
8. Y. L. Xiao and P. H. Liu, *Angew. Chem. Int. Edit.*, 2008, **47**, 9722-9725.
9. Y. L. Xiao, W. C. Chang, H. W. Liu and P. H. Liu, *Org. Lett.*, 2011, **13**, 5912-5915.
10. W. X. Wang, J. K. Li, K. Wang, C. C. Huang, Y. Zhang and E. Oldfield, *P. Natl. Acad. Sci. U.S.A.*, 2010, **107**, 11189-11193.
11. W. X. Wang, K. Wang, Y. L. Liu, J. H. No, J. K. Li, M. J. Nilges and E. Oldfield, *P. Natl. Acad. Sci. U.S.A.*, 2010, **107**, 4522-4527.
12. B. Altincicek, E. C. Duin, A. Reichenberg, R. Hedderich, A. K. Kollas, M. Hintz, S. Wagner, J. Wiesner, E. Beck and H. Jomaa, *FEBS Lett.,* 2002, **532**, 437-440.
13. I. Rekittke, J. Wiesner, R. Rohrich, U. Demmer, E. Warkentin, W. Y. Xu, K. Troschke, M. Hintz, J. H. No, E. C. Duin, E. Oldfield, H. Jomaa and U. Ermler, *J. Am. Chem. Soc.*, 2008, **130**, 17206-17207.
14. W. X. Wang, K. Wang, I. Span, J. Jauch, A. Bacher, M. Groll and E. Oldfield, *J. Am. Chem. Soc.*, 2012, **134**, 11225-11234.
15. S. Dapprich, I. Komaromi, K. S. Byun, K. Morokuma and M. J. Frisch, *J. Mol. Struc-Theochem.*, 1999, **461**, 1-21.
16. W. Deng, T. Vreven, M. J. Frisch and K. B. Wiberg, *J. Mol. Struc-Theochem.*, 2006, **775**, 93-99.
17. T. Vreven, K. S. Byun, I. Komaromi, S. Dapprich, J. A. Montgomery, K. Morokuma and M. J. Frisch, *Abstr. Pap. Am. Chem. S.*, 2006, **232**, 408-408.
18. S. Abdel-Azeim, X. Li, L. W. Chung and K. Morokuma, *J. Comput. Chem.*, 2011, **32**, 3154-3167.
19. V. Guallar and F. Wallrapp, *J. R. Soc. Interface*, 2008, **5**, S233-S239.
20. R. Z. Liao and W. Thiel, *J. Chem. Theory. Comput.*, 2012, **8**, 3793-3803.
21. C. L. Stanton, I. F. W. Kuo, C. J. Mundy, T. Laino and K. N. Houk, *J. Phys. Chem. B*, 2007, **111**, 12573-12581.
22. L. Noodleman and J. G. Norman, *J. Chem. Phys.*, 1979, **70**, 4903-4906.
23. L. Noodleman, *J. Chem. Phys.,* 1981, **74**, 5737-5743.
24. C. L. Fisher, J. Li, J. L. Chen, D. Bashford and L. Noodleman, *Abstr. Pap. Am. Chem. S.*, 1995, **209**, 153-COMP.
25. J. M. Mouesca, L. Noodleman and D. A. Case, *Int. J. Quantum Chem.*, 1995, **22**,95-102.
26. S. Q. Niu and T. Ichiye, *Abstr. Pap. Am. Chem. S.,* 2009, 238-238.
27. W.-G. Han, T. Lovell, T. Liu, L. Noodleman, *Inorg. Chem.* 2003, **42**, 5244-5251.
28. M. Chakrabarti, E. Munck and E. L. Bominaar, *Inorg. Chem.*, 2011, **50**, 4322-4326.
29. R. A. Torres, T. Lovell, L. Noodleman and D. A. Case, *J. Am. Chem. Soc.*, 2003, **125**, 1923-1936.
30. P. G. Blachly, G. M. Sandala, D. A. Giammona, T. Q. Liu, D. Bashford, J. A. McCammon and L. Noodleman, *J. Chem. Theory. Comput.,* 2014, **10**, 3871-3884.
31. B. F. Gherman, M. H. Baik, S. J. Lippard and R. A. Friesner, *J. Am. Chem. Soc.*, 2004, **126**, 2978-2990.
32. B. D. Dunietz, M. D. Beachy, Y. X. Cao, D. A. Whittington, S. J. Lippard and R. A. Friesner, *J. Am. Chem. Soc.*, 2000, **122**, 2828-2839.
33. T. Grawert, I. Span, W. Eisenreich, F. Rohdich, J. Eppinger, A. Bacher and M. Groll, *P. Natl. Acad. Sci. U.S.A.*, 2010, **107**, 1077-1081.
34. I. Span, K. Wang, W. X. Wang, Y. H. Zhang, A. Bacher, W. Eisenreich, K. Li, C. Schulz, E. Oldfield and M. Groll, *Nat. commun.,* 2012, **3**.
35. I. Span, K. Wang, W. X. Wang, J. Jauch, W. Eisenreich, A. Bacher, E. Oldfield and M. Groll, *Angew. Chem. Int. Edit.*, 2013, **52**, 2118-2121.
36. M. Bruschi, C. Greco, L. Bertini, P. Fantucci, U. Ryde and L. De Gioia, *J. Am. Chem. Soc.*, 2010, **132**, 4992–4993.
37. C. Greco, M. Bruschi, P. Fantucci, U. Ryde and L. De Gioia, *J. Am. Chem. Soc.*, 2011, **133**, 18742-18749.
38. X. B. Wang, S. Q. Niu, X. Yang, S. K. Ibrahim, C. J. Pickett, T. Ichiye and L. S. Wang, *J. Am. Chem. Soc.*, 2003, **125**, 14072-14081.
39. S. Q. Niu and T. Ichiye, *J. Am. Chem. Soc.*, 2009, **131**, 5724–5725.
40. H. J. Zhai, X. Yang, Y. J. Fu, X. B. Wang and L. S. Wang, *J. Am. Chem. Soc.*, 2004, **126**, 8413-8420.
41. F. Weinhold, *J. Comput. Chem.,* 2012, **33**, 2440-2449.
42. R. F. W. Bader, J. B. Russell, Clarendon Press: Oxford, U.K., 1990.
43. D. Chopra, *J. Phys. Chem. A*, 2012, **116**, 9791-9801.
44. C. F. Matta, R. J. , Wiley-VCH: Weinheim, 2007.
45. P. R. Varadwaj, A. Varadwaj and H. M. Marques, *J. Phys. Chem. A*, 2011, **115**, 5592-5601.
46. D. Rinaldo, D. M. Philipp, S. J. Lippard and R. A. Friesner, *J. Am. Chem. Soc.*, 2007, **129**, 3135-3147.
47. L. J. Farrugia, C. Evans and M. Tegel, *J. Phys. Chem. A,* 2006, **110**, 7952-7961.
48. P. R. Varadwaj, I. Cukrowski and H. M. Marques, *J. Phys. Chem. A,* 2008, **112**, 10657-10666.
49. L. J. Farrugia and H. M. Senn, *J. Phys. Chem. A,* 2010, **114**, 13418-13433.
50. T. Iwasaki, R. Fukazawa, Y. Miyajima-Nakano, A. Baldansuren, S. Matsushita, M. T. Lin, R. B. Gennis, K. Hasegawa, T. Kumasaka and S. A. Dikanov, J. Am. Chem. Soc., 2012, 134, 19731-19738.
51. X. Yang, S. Q. Niu, T. Ichiye and L. S. Wang, *J. Am. Chem. Soc.*, 2004, **126**, 15790-15794.
52. A. Sorkin, M. A. Iron and D. G. Truhlar, *J. Chem. Theory. Comput.*, 2008, **4**, 307-315.
53. J. Paier, R. Hirschl, M. Marsman and G. Kresse, *J. Chem. Phys.,* 2005, **122,** 234102-234113.
54. K. Janthawornpong, S. Krasutsky, P. Chaignon, M. Rohmer, C. D. Poulter and M. Seemann, *J. Am. Chem. Soc.,* 2013, **135**, 1816-1822.

55. F. Guerra, K. Wang, J. K. Li, W. X. Wang, Y. L. Liu, S. Amin and E. Oldfield, *Chem. Sci.*, 2014, **5**, 1642-1649.

Graphic Material for the Table of Contents